Unsteadiness and transition to turbulence in woven spacer filled channels for Membrane Distillation

To cite this article: M Ciofalo *et al* 2017 *J. Phys.: Conf. Ser.* **796** 012003

View the article online for updates and enhancements.

Unsteadiness and transition to turbulence in woven spacer filled channels for Membrane Distillation

M Ciofalo[*]**, F Ponzio, A Tamburini, A Cipollina, G Micale**
Dipartimento DICGIM, Università degli Studi di Palermo, Italy
[*]Corresponding author; email michele.ciofalo@unipa.it, tel. +39 091 232 225

Abstract. To characterize the performance of Membrane Distillation (MD) modules, channels filled with woven spacers were investigated by Computational Fluid Dynamics (including Direct Numerical Simulations and the use of the SST k-ω turbulence model) and by parallel experiments with Thermochromic Liquid Crystals. The cases considered here regard mutually orthogonal filaments with a spacer pitch to channel height ratio P/H=2, two spacer orientations θ with respect to the main flow (0° and 45°), and bulk Reynolds numbers Re from ~200 to ~2000, an interval of great interest in practical MD applications. For both values of θ, CFD predicted steady-state flow for Re up to ~300, and chaotic flow for Re larger than ~400. In the intermediate range Re≈300-400, periodic flow regimes were predicted for both orientations. These regimes were of particular interest and complexity, as they exhibited a slow global oscillation of the flow superimposed on high order harmonics corresponding to fast local oscillations. Experiments confirmed the appearance of unsteadiness for Re>~300. Heat transfer and friction were little affected by unsteadiness and exhibited a smooth behaviour with Re. The agreement with the experimental results was good using DNS, and acceptable using RANS.

1. Introduction and literature review

Spacers are widely used in a variety of membrane processes, among which Membrane Distillation (MD), both as structural elements and as mixing promoters, aimed at reducing polarization and enhancing heat or mass transport [1, 2, 3]. Unfortunately, they also cause pressure drop to increase [4]. Thus, much research effort has been devoted to the search for spacer configurations offering a compromise between heat / mass transfer and hydraulic losses [5, 6, 7, 8].

In recent years, Computational Fluid Dynamics (CFD) has increasingly been employed to this purpose. Once properly validated against experimental data, CFD provides valuable local information on both existing spacers and novel ones.

Early CFD efforts were limited to steady flow [9]. However, unlike other membrane processes such as Reverse Electrodialysis, characterized by very low Reynolds numbers and laminar or even creeping flow, MD usually involves Reynolds numbers up to a few thousand (see below for a precise definition of Re). Thus, an increasing number of CFD studies have been devoted to the simulation of unsteady flows. Limiting this brief survey to fully three-dimensional simulations (the only that can capture the complexity of the flow in a real spacer-filled channel), Koutsou *et al*. [10] performed Direct Numerical Simulations (DNS) with Fluent™, highlighting that unsteadiness may occur even at low Reynolds numbers, and Tamburini *et al*. [11] compared DNS results for early turbulent flow in channels filled with overlapped-type spacers, obtained by ANSYS-CFX™, with experimental measurements using Thermochromic Liquid Crystals. Mahdavifar *et al*. [12] performed DNS with OpenFOAM to investigate the effects of the spacer-to-wall clearance on the flow field; OpenFOAM

and DNS were also used by Mojab *et al*. [13] to simulate unsteady flow in channels equipped with overlapped spacers. At high Reynolds number, DNS can become too computationally expensive, and the use of a turbulence model may be more suitable. Thus, Shakaib *et al*. [14] employed the Spalart-Allmaras model (based on a single transport equation for the turbulent viscosity) to predict temperature polarization in membrane distillation modules.

2. Configuration studied and main definitions

The spacer geometry considered in the present study is illustrated in Figure 1, and consists of mutually orthogonal cylindrical filaments of diameter δ, arranged in a woven pattern with pitch P. Figure 1(a) shows the physical spacer model used in the experimental tests, characterized by δ=5×10^{-3} m and P=2×10^{-2} m. Figure 1(b) shows the unit cell chosen as the computational domain in the numerical simulations; and Figure 1(c) shows a particular of the computational grid, consisting of both hexahedral and tetrahedral volumes. Since the pitch to filament diameter ratio is P/δ=4 and the channel height is H=2δ (neglecting the small deformation of the filaments at the contact points between one another and with the walls), the spacer pitch to channel height ratio is P/H=2.
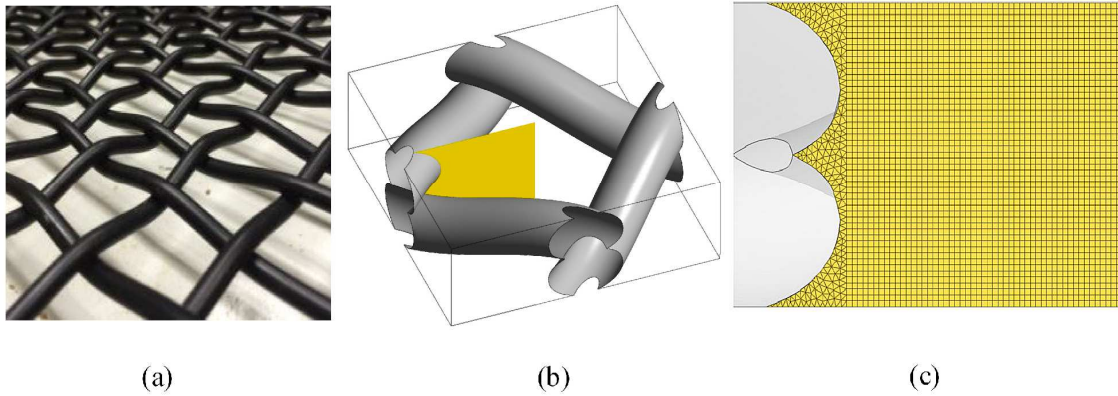

(a)   (b)   (c)

Figure 1. Woven spacer configuration examined in the present study. (a) Physical model used in the experiments; (b) unit cell for CFD; (c) computational grid in the region highlighted in (b).

As in our previous paper [11], dimensionless quantities are defined with reference to the void (spacerless) configuration, i.e. to a plane channel having height H and thus hydraulic diameter D_h=2H. Coherently, the bulk Reynolds number is

$$\mathrm{Re} = U \cdot 2H / \nu \tag{1}$$

in which $U = Q/(WH)$ is the mean "void channel" streamwise velocity, Q being the volume flow rate and W the channel's spanwise extent (in the experiments, H = 0.01 m and W = 0.22 m). We prefer this definition, adopted also by other authors [15], to that based on the actual hydraulic diameter and mean velocity, because it makes comparisons between different configurations more meaningful.

The friction velocity Reynolds number Re_τ is defined as

$$\mathrm{Re}_\tau = u_\tau (H/2) / \nu \tag{2}$$

in which $u_\tau = (\langle \tau_w \rangle / \rho)^{1/2}$ is the friction velocity. The quantity $\langle \tau_w \rangle$ is the wall-averaged wall shear stress which, in a void plane channel and under steady-state conditions, would balance the large-scale pressure gradient along the main flow direction ξ, defined as $p_\xi = -\Delta p / \Delta \xi$, so that $\langle \tau_w \rangle = (H/2) p_\xi$.

The Darcy friction coefficient (four times the Fanning friction factor) is defined as

$$f_D = \frac{4H}{\rho U^2} p_\xi \tag{3}$$

On the basis of the definitions given above for Re and Re_τ, one has also f_D=128(Re$_\tau$/ Re)^2. The

local Nusselt number is defined as

$$Nu = h\frac{2H}{\lambda} \tag{4}$$

in which $h=q''_w/(T_b-T_w)$ is the local heat transfer coefficient, T_b is the fluid bulk temperature in the unit cell and T_w is the local wall temperature. Wall-averaged values will be indicated as $\langle h \rangle$ and $\langle Nu \rangle$. The Prandtl number was assumed to be 4.63, representative of water at 39°C.

Woven spacers have been studied far less in depth than non-woven ones. They are often mentioned in connection with different membrane-based processes [6, 16, 17, 18], but no systematic analysis, either experimental or computational, of their performance regarding pressure drop and heat / mass transfer seems to have been performed. What can be said with some confidence is that woven spacers provide larger heat / mass transfer coefficients, but also higher pressure drops, than overlapped ones. Our group has recently performed experimental measurements and CFD simulations on woven spacers for Membrane Distillation with different values of the spacer pitch to channel height ratio, working at bulk Reynolds numbers up to 2000 [19]; this study follows a similar experimental and computational investigation on overlapped (non-woven) spacers [8, 11, 20, 21, 22, 23].

3. Experimental method
The experimental apparatus has been described in detail in previous papers [23]. Experiments were conducted on a scaled-up spacer-channel configuration, Figure 1(a), purpose manufactured from commercial black rubber wire 5 mm in diameter. The resulting distance between the plane channel walls was ~10 mm. The pitch of the wire net was ~20 mm, giving a pitch-to-height ratio *P/H* of ~2.

The use of Thermochromic Liquid Crystals (TLC) to obtain surface temperature distributions [24] or even three-dimensional temperature and flow fields [25] is amply documented in the scientific literature [24]. Images of the TLC-covered wall were split into HSV (Hue, Saturation, Value) components, of which only H was used to derive the wall temperature on the basis of an *in situ* calibration, performed by the isothermal method. For the TLC preparation used here (Hallcrest™ R30C5W) the nominal colour play (from red start to blue start) was 30-35°C while the actual resolved temperature range was ~31-46°C.
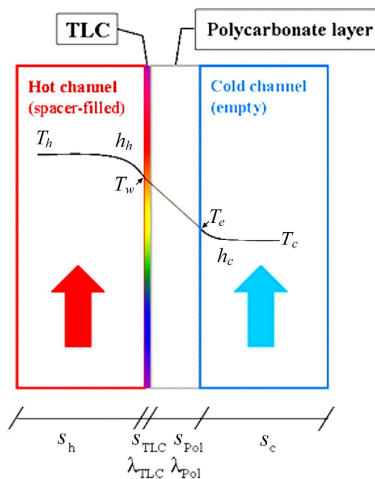

Figure 2. Sketch of the temperature profile across the different layers of the test section.

Figure 2 reports a schematic representation of the temperature profile across the different layers of the test section including a hot channel, a TLC sheet, a dividing wall made of 1 mm thick polycarbonate, and a cold channel. An elementary analysis of the heat transfer process occurring through the various layers in series, under the assumption of one-dimensional transport (demonstrated to be reliable in [23]), gives the local hot-side heat transfer coefficient *h* as a function of the locally

measured temperature T_w of the TLC sheet once the bulk temperatures T_h, T_c and the cold-side heat transfer coefficient are known:

$$h = \frac{1}{r}\frac{T_w - T_c}{T_h - T_w}$$
(5)

Here, r is an overall external thermal resistance consisting of the conductive thermal resistances s/λ of the thermochromic liquid crystal film (*TLC*) and of the polycarbonate layer (*pol*), in series with the convective thermal resistance $1/h_c$ associated with the cold channel:

$$r = \frac{s_{TLC}}{\lambda_{TLC}} + \frac{s_{pol}}{\lambda_{pol}} + \frac{1}{h_c}$$
(6)

T_h and T_c were measured by Pt100 RTDs at the inlet and outlet of the hot and cold channels and a linear variation of T_h and T_c along the flow direction was assumed, as justified by the fact that estimated relaxation lengths are far larger than the test section length. The cold-side convection coefficient h_c was estimated by the Dittus-Bölter correlation (Nu=0.023 Re$^{0.8}$ Pr$^{0.4}$) written for turbulent flow in the cold channel; a sensitivity analysis showed that the value of h calculated by Eq. (5) is only a weak function of the value used for h_c. The value of $6.24 \cdot 10^{-3}$ m^{2}K/W was computed for the overall thermal resistance r, and h was then expressed in dimensionless form as Nu=hd_{eq}/λ.

As an example of the information that can be extracted from the pictures by digital image processing, Figure 3 reports unit cell distributions obtained for P/H=2, θ=90° and a flow rate of ~60 l/h (yielding a bulk Reynolds number Re≈215). The flow is from left to right. Graph (a) is a picture of the active, TLC-covered wall, in which saturation was enhanced for clarity purposes; the arrow indicates the main flow direction. Graph (b) shows the distribution of the local Nusselt number Nu, derived by digitally processing the image in (a).
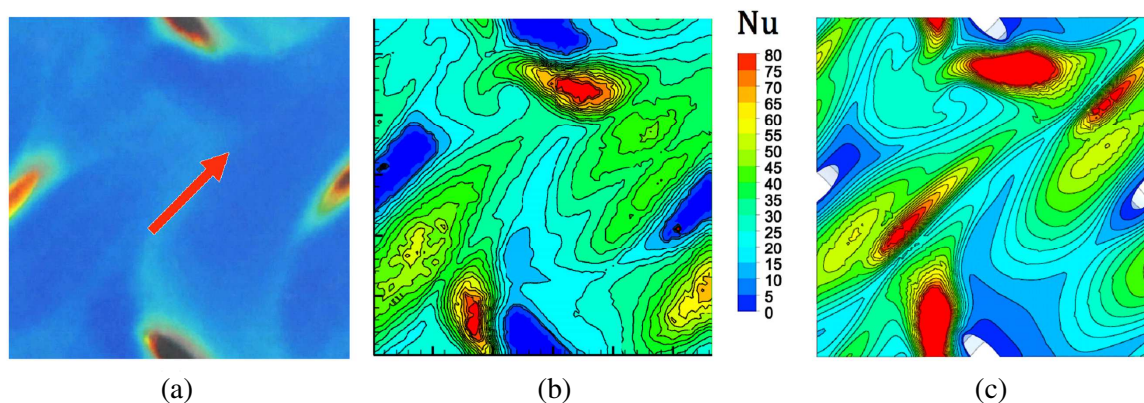

(a)   (b)   (c)

Figure 3. Unit cell of a woven spacer (P/H=2, θ=0-90°, Re≈215). (a) picture of the TLC-covered wall (the arrow indicates the flow direction); (b) local Nusselt number Nu; (c) DNS results for Re$_\tau$=80, yielding Re≈240.

The analysis of short movies of the TLC-covered wall revealed that the colour (i.e., wall temperature) pattern was almost steady below a bulk Reynolds number of ~300 and clearly unsteady at larger values of Re. This is illustrated in Figure 4 by reporting three frames, separated by a few seconds, for each of the two Reynolds numbers 255 and 921.

Pressure drops in the hot fluid side were measured by using two longitudinally spaced tappings, located along the test section mid-line and 50 cm apart, and a Fuji Electric FCX-AII™ differential manometer with a response of ~7.4 µA/Pa. Pressure drops were generally very small (e.g. 25 Pa at Re=350) and thus could be measured only with a limited accuracy.
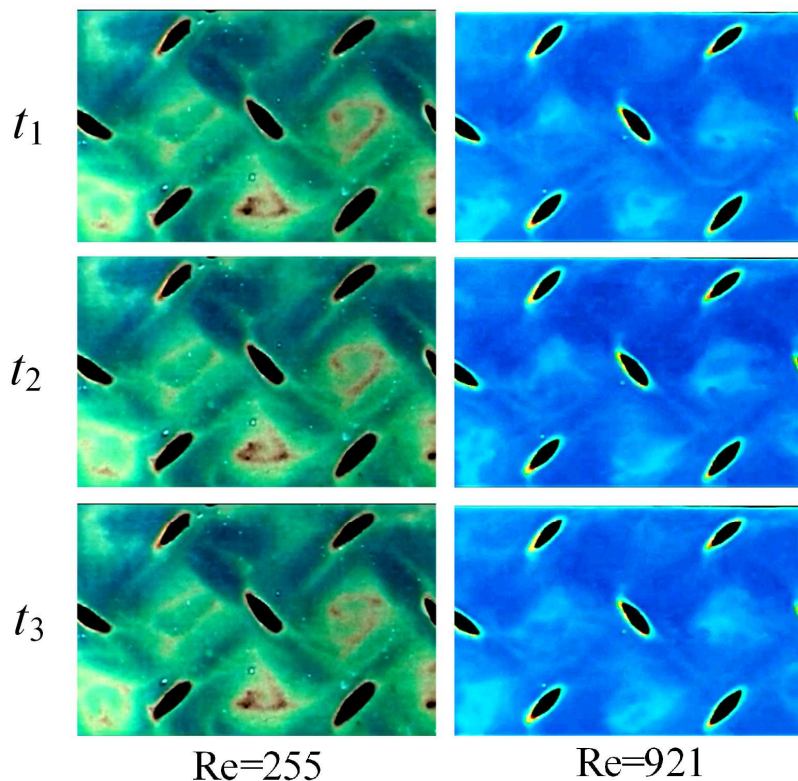
Figure 4. Photographs of the TLC-covered wall taken at three instants t_1-t_2-t_3 (separated by a few seconds) for θ=45° and two Reynolds numbers, showing substantial steadiness for Re=255 and large unsteadiness for Re=921. Images were processed so as to enhance the differences between frames.

4. Computational method

The computational domain was the unit, periodic cell shown in Figure 1(b). Mathematically, the problem was described by the continuity, Navier-Stokes and energy equations for a constant-property fluid. The "unit cell" treatment, first described by our group in ref. [26], allowed periodicity conditions to be adopted for all variables at the opposite faces of the computational domain. The friction Reynolds number Re_τ(i.e., the pressure drop per unit length) was imposed, while the bulk Reynolds number (i.e., the flow rate) was computed as part of the solution. All simulations were conducted by the finite volume ANSYS-CFX14™ code [27].

No slip conditions (u_i=0) were imposed at the walls and on the filaments' surface. In regards to the thermal boundary conditions, the bottom wall and the filaments were assumed to be adiabatic ($q"$=0), while at the top (thermally active) wall a third-type (mixed) condition was imposed:

$$T_w - T_c = r \, q"_w \tag{7}$$

mimicking the experimental boundary condition. Values representative of those holding in the experiments were chosen for the outer temperature T_c and the thermal resistance r (19°C and 6.24·10^{-3} m^{2}K/W, respectively). Also the spacer dimensions were the same as the experimental ones and the fluid was assumed to be water at 39°C with physical properties ρ=992.5 kg/m^3, c_p=4179 J/(kgK), λ=0.5985 W/(mK), μ=6.625×10^{-4} Pa·m, yielding Pr=4.63. Finally, as in the experiments, two orientations of the main flow with respect to the spacer filaments of the upper layer were considered (0° and 45°). In the present study, all simulations were run in time-dependent mode and attained either a steady-state or a time-dependent (time periodic or irregular, i.e. chaotic) regime.

Unlike the corresponding overlapped-spacer geometry [11], the present one could not be discretized with purely hexahedral volumes; a hybrid grid was thus built, in which tetrahedral volumes were used in the regions surrounding the filaments (~30% of the overall volume of the computational domain) and hexahedral volumes in the remaining regions. Figure 1(c) reports a detail of the mesh.
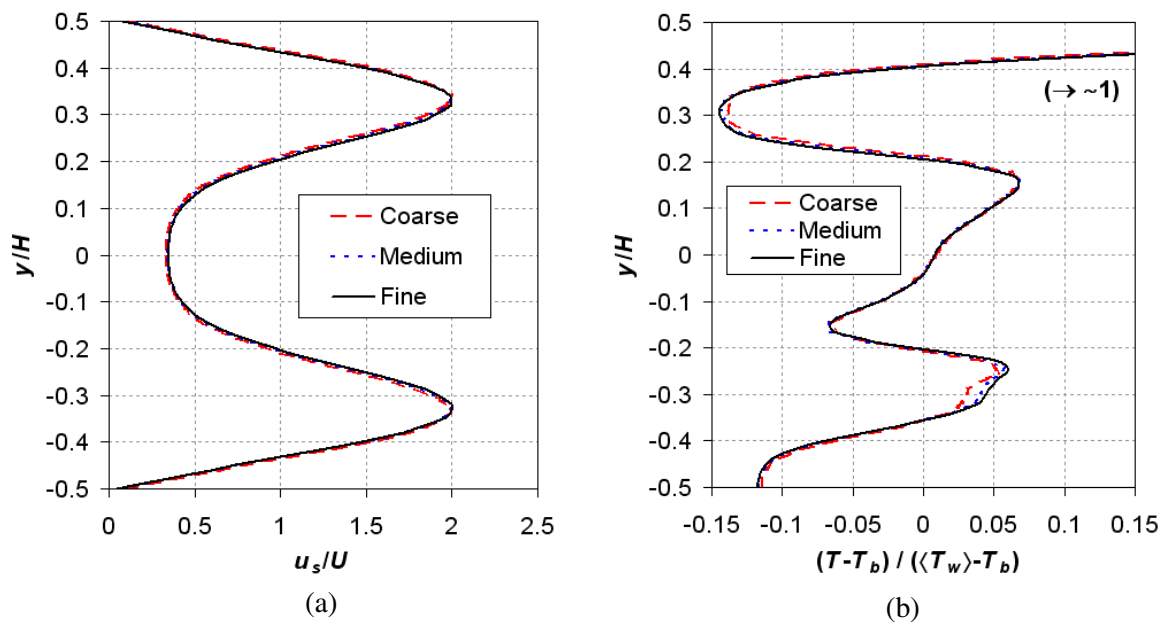
Figure 5. Grid sensitivity: profiles of normalized streamwise velocity u_s (a) and temperature T (b) along a line perpendicular to the walls and passing by the centroid of the unit cell, as computed for θ=45°, Re_τ=70 by using three different grids with ~0.84×10^6 (coarse), ~2.00×10^6 (medium) and ~3.49×10^6 (fine) volumes.

A grid sensitivity study was conducted for θ=45°, Re_τ=70 (steady-state flow at Re=273). Figure 5 reports the profiles of normalized streamwise velocity u_s (a) and temperature T (b) along a line perpendicular to the walls and passing by the centroid of the unit cell, as computed by using three grids with ~0.84×10^6, ~2.00×10^6 and ~3.49×10^6 volumes, respectively. As it can be observed, the results from the two finer grids are almost identical, and even the coarsest grid provides very similar results. For the final simulations, the intermediate grid of ~2×10^6 finite volumes was adopted.

5. Results

5.1 Case θ=0-90°
For this orientation (main flow parallel and orthogonal to the two filament layers), steady-state flow was predicted for Re_τ up to ~105 (Re up to ~340), periodic flow for Re_τ≈110 (Re≈350) and chaotic flow for Re_τ≈120 or larger (Re≥~390).

As an example of steady-state results, Figure 3(c) reports, along with experimental results obtained under similar conditions, the local Nusselt number distribution predicted for Re_τ=80, yielding Re≈240. A good general agreement can be observed. The main differences regard the values of Nu maxima, which are somewhat overestimated by the numerical simulations, and the narrow regions of high Nu predicted by CFD along the diagonal parallel to the main flow, not present in the experiments.

As an example of periodic behaviour, Figure 6(a) reports a time series of the streamwise velocity u_s at the centre of the unit cell for Re_τ=110, or Re≈352 (velocity is normalized by the mean streamwise velocity U, time by δ/U). The time interval showed includes three periods; the duration T_0 of each period is ~100 δ/U, corresponding to ~42 s at the scale of the experiments. Graph (b) reports an enhanced detail of the behaviour of u_s in the shorter interval highlighted in (a), showing a secondary "quasi-period" of ~ T_0/100 which corresponds to 1× δ/U, or ~0.42 s at the scale of the experiments.

The corresponding power spectrum is reported in Figure 7; here, frequency is normalized as $F=f/(U/\delta)$, i.e. as a Strouhal number based on mean velocity and filament diameter, while P_{uu} is in arbitrary units. Discrete peaks, corresponding to a base dimensionless frequency F_0 of ~0.01 and its harmonics, are visible; the very high order harmonic at 105 F_0 corresponds to the rapid oscillations in Figure 6(b).
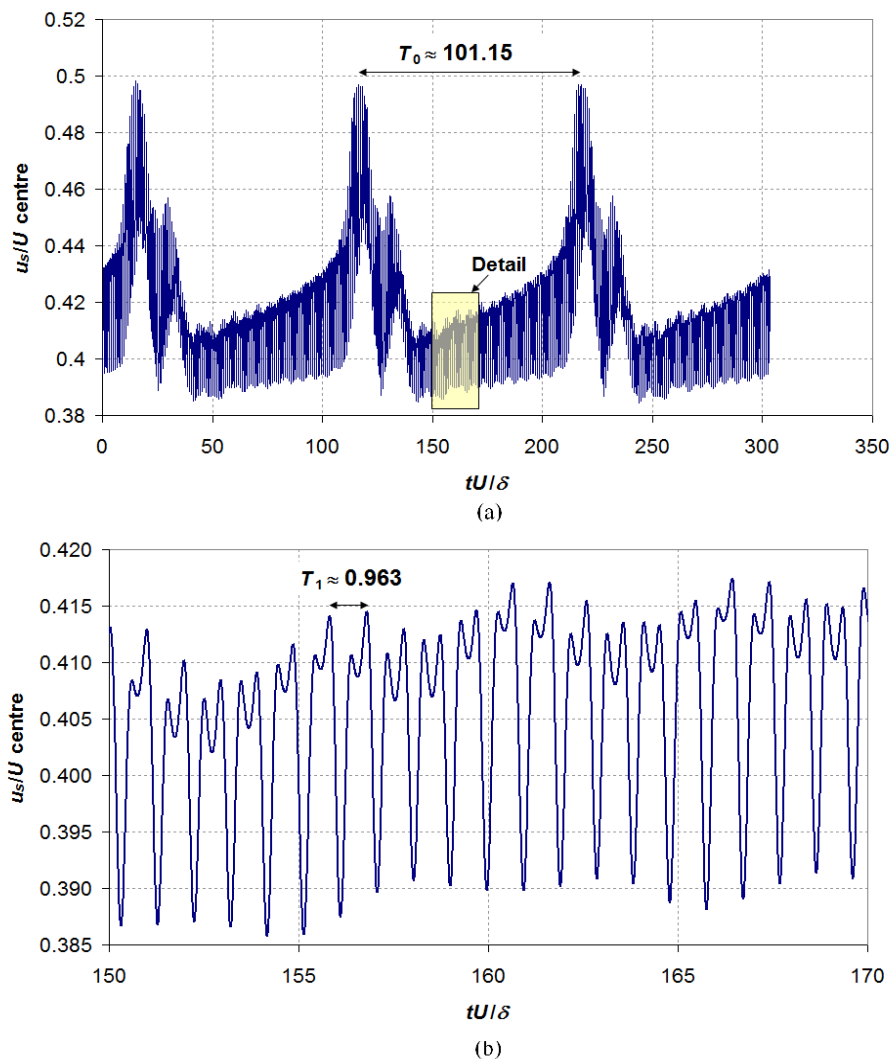
Figure 6. Time series of the streamwise velocity u_s at the centre of the unit cell for θ=0-90° and Re$_\tau$=110 (Re=352, periodic flow). Velocity is normalized by the mean streamwise velocity U, time by δ/U. (a) Large scale behaviour over a time interval including three periods T_0. (b) Detail of the behavior of u_s in the interval highlighted in (a), showing a secondary "quasi-period" of ~ T_0/100.

Finally, as an example of fully chaotic behaviour, Figure 8 reports computational results for θ=0-90° and Re$_\tau$=140 (Re=478): graph (a) shows a time series of the streamwise velocity u_s at the centre of the unit cell, while graph (b) is the corresponding time power spectrum. All quantities are normalized as in Figures 6 and 7. It can be observed that velocity fluctuations are irregular and that their spectrum includes a large number of independent frequencies, but a frequency interval exhibiting the characteristic -5/3 power law behaviour of full turbulence (inertial sub-range) is barely identifiable.

5.2 Case θ=45°
For this orientation (main flow bisecting the angle formed by the two filament layers), steady-state flow was predicted for Re$_\tau$ up to ~70 (Re up to ~225), periodic flow for Re$_\tau\approx$80-100 (Re$\approx$270-365) and chaotic flow for Re$_\tau\approx$120 or larger (Re$\geq$~465).
For the sake of brevity, representative steady-state results are not reported. As an example of periodic behaviour, Figure 9(a) reports a time series of the streamwise velocity u_s at the centre of the unit cell for Re$_\tau$=100, or Re$\approx$365. Figure 9(b) reports the corresponding power spectrum. Time, velocity and frequency are normalized as in the previous Figures 6-8.
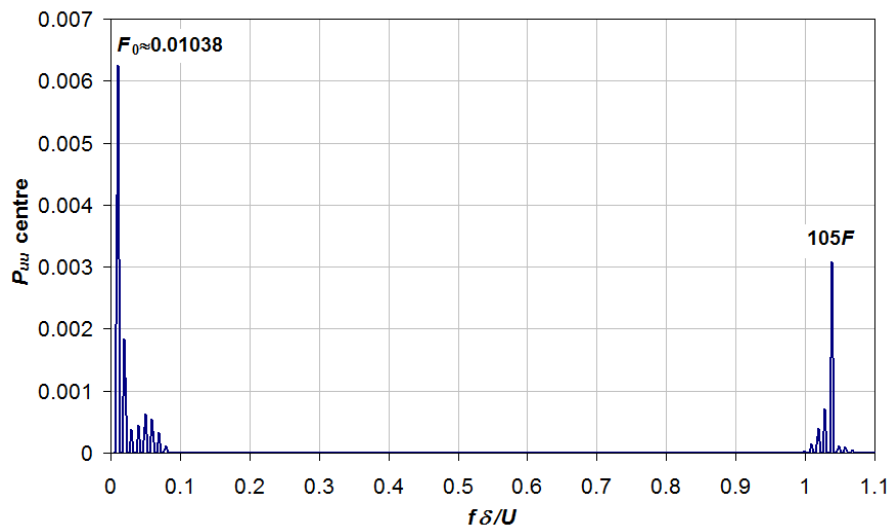
Figure 7. Power spectrum of the streamwise velocity u_s at the centre of the unit cell for θ=0-90° and Re_τ=110 (Re=352), reported as a function of time in Figure 6 (frequency is normalized by U/δ, i.e. as a Strouhal number, while P_{uu} is in arbitrary units).

The time interval considered in Figure 9 includes three periods, each of duration $T_0 \approx 6.5 \delta/U$ (corresponding to ~2.65 s at the scale of the experiments). In the spectral density diagram, this periodicity corresponds to the base frequency $F_0 \approx 0.15$. However, most of the fluctuation intensity is associated with a secondary period $T_1 = T_0/5$ (i.e., ~1.3δ/U, or ~0.53 s at the scale of the experiments), corresponding to the spectral peak at $F_1 = 5F_0$. Harmonics at 4, 6 and 9 × F_0 are also appreciable.

Finally, an example of fully chaotic behaviour is reported also for the 45° orientation in Figure 10, which is for Re_τ=120 (Re=465). The quantities reported are the same as in Figure 8, and time series and spectra are similar. In this latter case, the power spectrum P_{uu} in Figure 10(a) exhibits a marked peak at $f\delta/U \approx 2.3$ which does not have a clear counterpart in the case θ=0-90° of Figure 8.

5.3 Bifurcation diagram

On the basis of the simulations performed, the tentative bifurcation map in Figure 11 can be drawn. It reports the rms value of the fluctuating streamwise velocity, u_{rms}, at the centre of the computational domain (normalized, as usual, by U) as a function of the Reynolds number Re for both flow attack angles. Symbols correspond to actual computational results (S: steady-state flow; P: periodic flow; C: chaotic flow). Shaded circles indicate the presumable position of bifurcations from steady to periodic or from periodic to chaotic flow.

Of course, one has u_{rms}=0 for all steady-state solutions. For θ=45°, the periodic branch bifurcates from the steady-state one at Re≈225 and extends above Re=350; the amplitude of the fluctuations increases considerably in this range. A second bifurcation from time-periodic to chaotic flow must occur at slightly higher Re, and is accompanied by a reduction of the velocity fluctuation amplitude. For θ=0-90°, the periodic branch bifurcates from the steady-state one at some Re intermediate between ~330 and ~350 but is rather short, probably ending at Re=370-380; a further bifurcation leads to a chaotic flow branch exhibiting, at least in the range studied here, a monotonic increase of the velocity fluctuation amplitude. All bifurcations appear to be of the supercritical type, i.e. they are not associated to abrupt changes in the computed quantities.
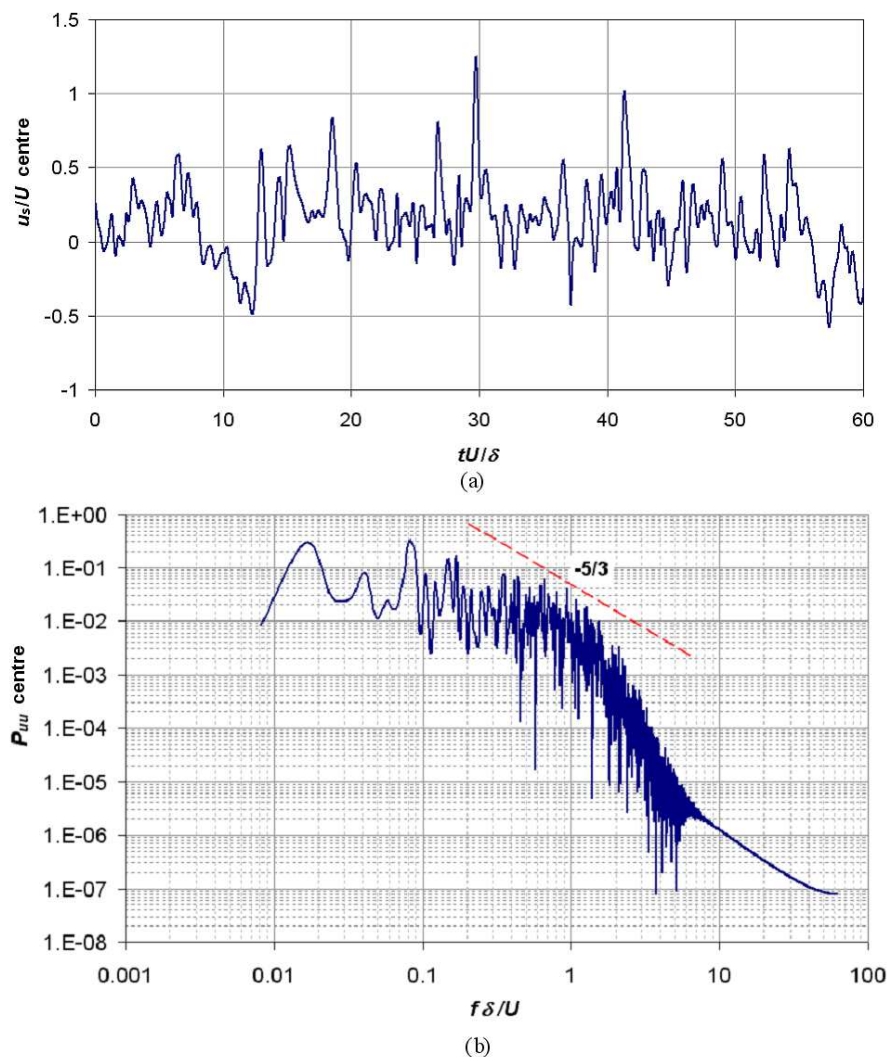
(a)

(b)

Figure 8. Computational results for $\theta=0\text{-}90°$ and $\mathrm{Re}_\tau=140$ (Re=478, chaotic flow). (a) Behavior of the streamwise velocity u_s at the centre of the unit cell (u_s is normalized by the mean streamwise velocity U, time by δ/U). (b) Corresponding power spectrum (frequency is normalized by U/δ, i.e. as a Strouhal number, while P_{uu} is in arbitrary units).

6. Comparison of experimental and computational results

6.1 Pressure drop

Figure 12 reports the Darcy friction coefficient f (normalized by that for parallel flow in a plane channel, 96/Re) both for $\theta=0\text{-}90°$ (a) and for $\theta=45°$ (b). Experimental results are shown along with computational ones, obtained either by direct numerical simulation or by a RANS turbulence model. In the case of time-dependent (periodic or chaotic) DNS solutions, f was computed as a time average. RANS simulations were run in steady-state mode; the SST model [28] was chosen not only because it is one of the best established turbulence models for general-purpose applications (at least among the two-equation, eddy diffusivity models), but also because, in a preliminary comparative study for the present spacer-filled channel configuration, it performed far better than alternative models including the two-equation RNG $k\text{-}\varepsilon$ and the second-order SSG.

A first noteworthy feature of Figure 12 is that neither experimental results nor computational ones (DNS or RANS) exhibit any significant change of value or slope in correspondence with the transition from steady to unsteady flow (which, according to the DNS summary results reported in Figure 11, occurs at Re≈340 for $\theta=0\text{-}90°$ and at Re≈225 for $\theta=45°$).
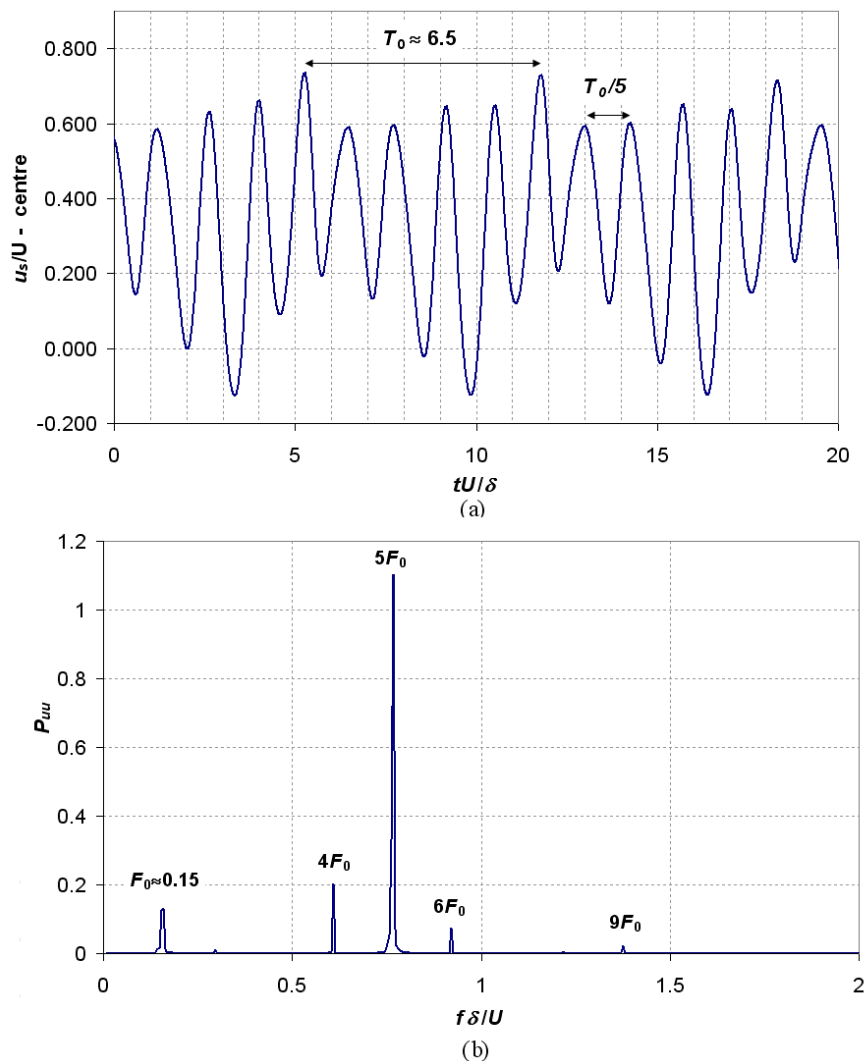
9

Figure 9. Computational results for θ=45° and Re_τ=100 (Re=365, periodic flow). (a) Behavior of the streamwise velocity u_s at the centre of the unit cell (u_s is normalized by the mean streamwise velocity U, time by δ/U). (b) Corresponding power spectrum (frequency is normalized by U/δ, i.e. as a Strouhal number, while P_{uu} is in arbitrary units).

Also the transition from periodic to chaotic flow (occurring at Re≈375 both for θ=0-90° and for θ=45° according to the map in Figure 11) is not reflected in any visible feature of the results. Note that the lack of large-scale effects (i.e., effects on the f *vs*. Re and ⟨Nu⟩ *vs*. Re curves) in correspondence with the loss of stability of stationary or periodic regimes is a feature common to many problems characterized (like the present one) by some geometrical complexity and by the existence of significant secondary flow even at low-Re. For example, it was observed both experimentally and by DNS in curved and helical pipes [29].

Both for θ=0-90° and for θ=45°, the agreement between experimental and DNS results is good in the limited ranges of overlap (Re up to ~500). For both values of θ, SST simulations underpredict the experimental results. For θ=0-90°, graph (a), the relative discrepancy remains limited (~10%) up to Re≈700, but becomes larger at the highest Re. For θ=45°, graph (b), the relative underprediction remains of the order of 20% over the whole range investigated but SST results exhibit a slight discontinuity at Re just above 1000, associated with the transition from a poor and slow convergence at lower Re to a better and faster convergence at higher Re.
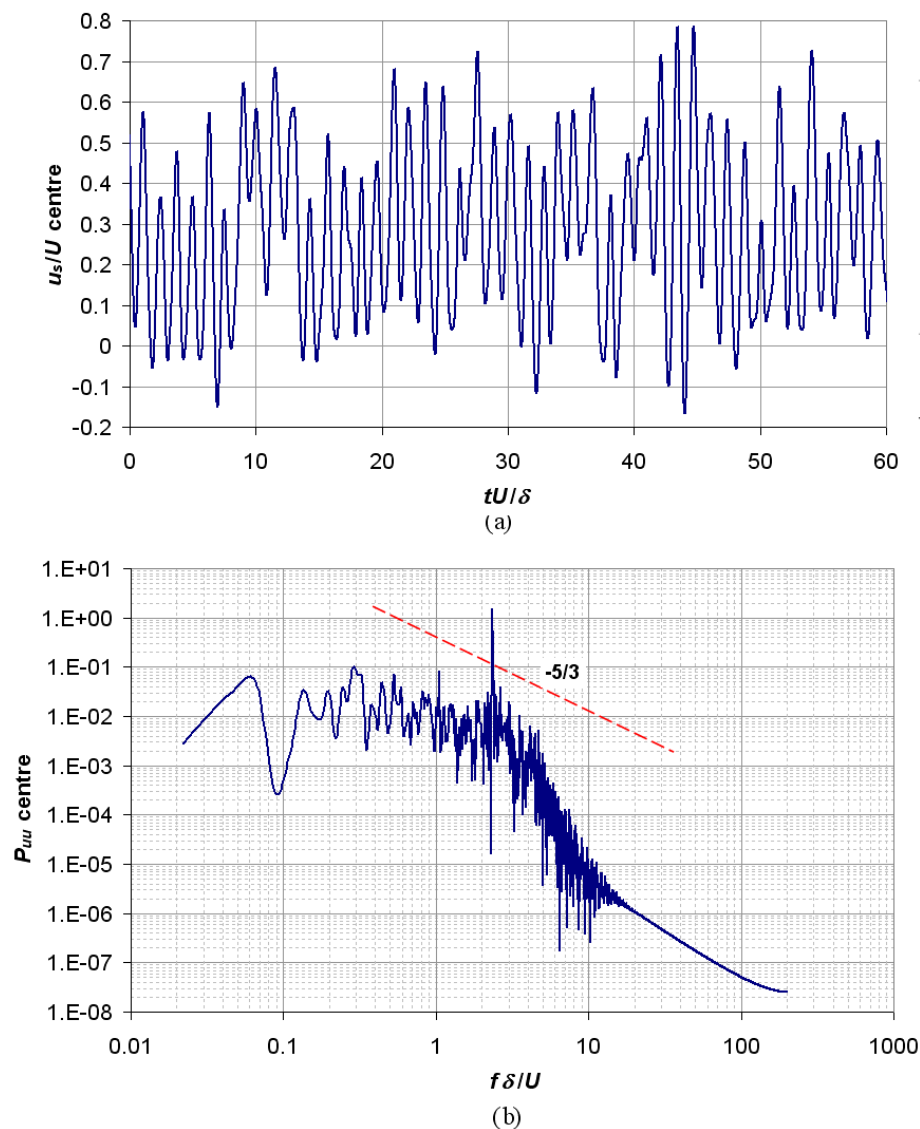
Figure 10. Computational results for $\theta=45°$ and $Re_\tau=120$ (Re=465, chaotic flow). (a) Behavior of the streamwise velocity u_s at the centre of the unit cell (u_s is normalized by the mean streamwise velocity U, time by δ/U). (b) Corresponding power spectrum (frequency is normalized by U/δ, i.e. as a Strouhal number, while P_{uu} is in arbitrary units).

This discontinuity seems to have little to do with the transition from steady to unsteady or from periodic to chaotic flow, discussed a few lines above; it occurs at much higher Re and regards only RANS results which are all for steady-state conditions by definition. Moreover, no discontinuity was observed in the RANS results for $\theta=0$-$90°$. Either computational results for creeping flow or an extrapolation of the experimental results to Re=0 indicate that, for very low Re, the friction coefficient is enhanced about 14.6 times by the presence of the spacer.

6.2 Heat transfer
Figure 13 reports the wall-averaged Nusselt number $\langle Nu \rangle$ both for $\theta=0$-$90°$ (a) and for $\theta=45°$ (b). As in Figure 12, experimental results are shown along with computational ones, obtained by direct numerical simulation or by steady-state SST simulations. As for f, in the case of time-dependent DNS results $\langle Nu \rangle$ was computed as a time average.
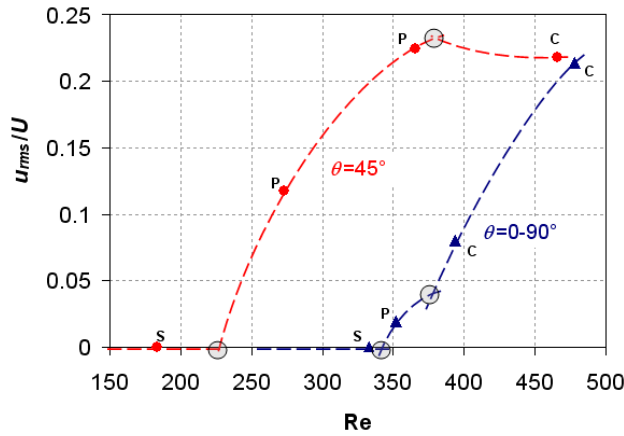
Figure 11. Tentative bifurcation diagram reporting the rms streamwise velocity fluctuation u_{rms} at a monitoring point (normalized by the mean streamwise velocity U) as a function of the Reynolds number Re. Symbols correspond to computational results (S: steady-state flow; P: periodic flow; C: chaotic flow). Shaded circles indicate bifurcations from steady to periodic or from periodic to chaotic flow.
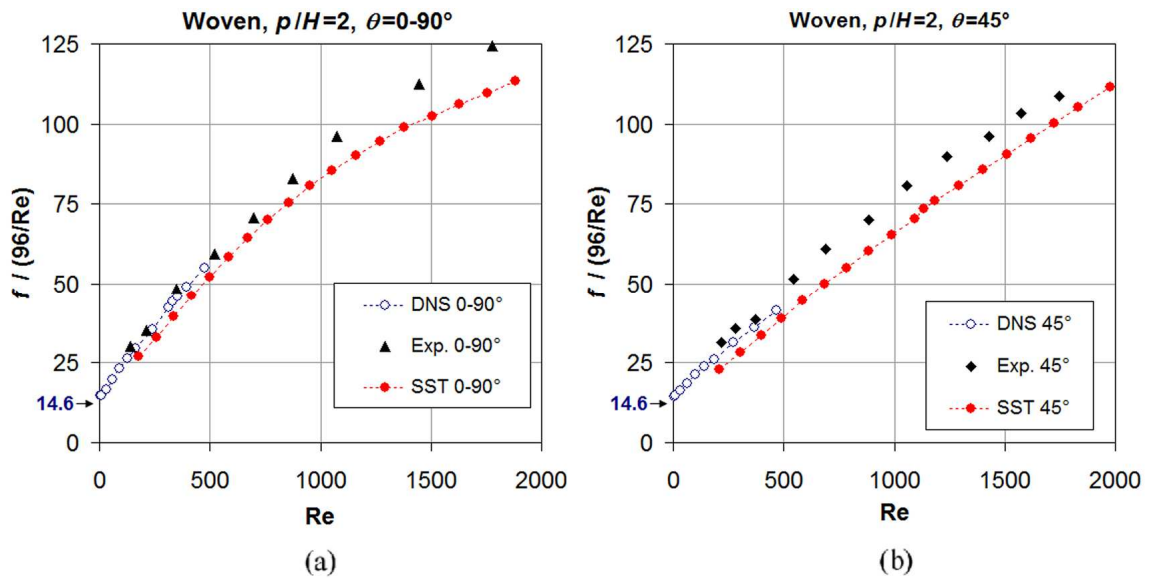

Figure 12. Friction coefficient (normalized by that for parallel flow in a plane channel, 96/Re): experimental results along with computational results obtained by DNS and by the SST model. (a) θ=0-90°; (b) θ=45°.
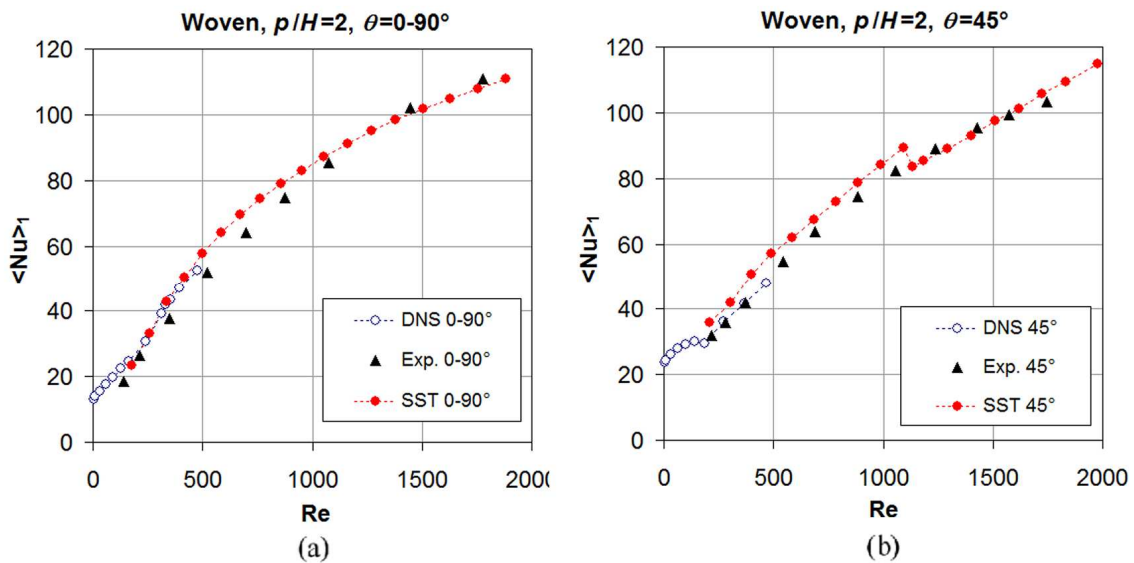

Figure 13. Wall-averaged Nusselt number: experimental results along with computational results obtained by DNS and by the SST model. (a) θ=0-90°; (b) θ=45°.

The remarks on the lack of features associated with the transitions from steady to unsteady flow and from periodic to chaotic solutions, made for the friction coefficient (see Figure 12 and Section 6.1 above), apply also to the Nusselt number in Figure 13.

In the limited range of overlap (Re up to ~500), the agreement between experimental and DNS results is excellent for θ=45° (b) and good, with some slight overprediction, for θ=0-90° (a). For both angles, SST simulations yield some overprediction (max. 15%) of the experimental results up to Re=1000-1300, while a better agreement is obtained for larger Re. As in Figure 12, the SST results for θ=45° (but not those for θ=0-90°) exhibit a small discontinuity for Re just above 1000, in correspondence with the transition from a poor convergence at low Re to a better one at high Re.

7. Conclusions

The aim of the present work was to answer the following questions, which are all of some considerable importance for the optimum design of Membrane Distillation modules and their spacers:

I)   In the complex geometry of a woven spacer filled channel, what are the possible flow regimes, the associated Reynolds number ranges and the modes of transition from a regime to another?

II)   How do these transitions affect friction and heat transfer?

III) Is there a computational approach capable of reproducing experimental data through the whole Reynolds number range of interest for MD applications (say, 200 to 2000)?

To the first of these questions, the answer is provided by DNS (with the partial support of experimental work). This shows that *transition from steady to unsteady flow occurs via a first bifurcation from steady to time-periodic flow, followed by a second one from periodic to chaotic flow*. Both bifurcations are of the supercritical type, so that they do not imply either abrupt jumps in the flow quantities or hysteresis phenomena. The critical values of Re, and the relative extent of the different regime ranges, vary with the flow attack angle; in particular, periodic flow was found to exist in a small range of Re (340~375) for θ=0-90°, but in a much broader range (225~375) for θ=45°.

To the second question, the answer is that *unsteadiness and turbulence affect only marginally and indirectly both friction and heat transfer*, which are dominated by the features of the mean flow and, in particular, by the spacer-induced recirculation. The intensity of this latter increases with Re, but does not exhibit any abrupt jump in correspondence with flow regime transitions, as proved by the fact that both the *f vs.* Re and the ⟨Nu⟩ *vs.* Re curves (as derived either from experiments or from DNS) are smooth in the whole Reynolds number range investigated (0~2000).

Finally, the answer to the third question is that *the only computational approach providing an excellent prediction of experimental results is direct numerical simulation*, which, however, becomes highly computationally demanding in turbulent flow (Re>~400). Among the various RANS models tested (including RNG k-ε, SST k-ω and second-order Reynolds stress transport models), *SST provided the best results*. Even SST, however, exhibited shortcomings including a significant underprediction (10-20%) of the friction coefficient, a poor convergence for Re<~1000, and an abrupt, although limited, jump in *f* and ⟨Nu⟩ across Re≈1000 for θ=45°. Despite these drawbacks, SST allowed acceptably accurate results to be computed through the whole Re range of interest, and correctly predicted laminarization at low Re without the need for external "*ad hoc*" input.

References

[1]   L. Martínez-Díez, M.I. Vázquez-González, Temperature and concentration polarization in membrane distillation of aqueous salt solutions, *J. Membr. Sci.*, 156 (1999) 265-273.

[2]   J. Schwinge, P.R. Neal, D.E. Wiley, D.F. Fletcher, A.G. Fane, Spiral wound modules and spacers: Review and analysis, *J. Membr. Sci.*, 242 (2004) 129–153.

[3]   M. Amokrane, D. Sadaoui, C.P. Koutsou, A.J. Karabelas, M. Dudeck, A study of flow field and concentration polarization evolution in membrane channels with two-dimensional spacers during water desalination, *J. Membr. Sci.*, 477 (2015) 139-150.

[4]   G. Schock, A. Miquel, Mass transfer and pressure loss in spiral wound modules, *Desalination*, 64 (1987) 339-352.

[5]   J. Phattaranawik, R. Jiraratananon, A.G. Fane, C. Halim, Mass flux enhancement using filled channels in Direct Contact Membrane Distillation, *J. Membr. Sci.*, (2001) 193-201.

[6] F. Li, W. Meindersma, A.B. de Haan, T. Reith, Optimization of commercial net spacers in spiral wound membrane modules, *J. Membr. Sci.*, 208 (2002) 289–302.

[7] Y. Yun, J. Wang, R. Ma, A.G. Fane, Effects of channel spacers on Direct Contact Membrane Distillation, *Desalination and Water Treatment*, 34 (2011) 63-69.

[8] A. Tamburini, A. Cipollina, S. Al-Sharif, M. Albeyrutty, L. Gurreri, G. Micale and M. Ciofalo, Assessment of temperature polarization in Membrane Distillation channels by Liquid Crystal Thermography, *Desalination and Water Treatment*, 55 (2015) 2747-2765.

[9] S.K. Karode, A. Kumar, Flow visualization through spacer filled channels by computational fluid dynamics I. Pressure drop and shear rate calculations for flat sheet geometry, *J. Membr. Sci.*, 193 (2001) 69–84.

[10] C.P. Koutsou, S.G. Yiantsios, A.J. Karabelas, Direct numerical simulation of flow in spacer-filled channels: effect of spacer geometrical characteristics, *J. Membr. Sci.*, 291 (2007) 53–69.

[11] A. Tamburini, M. Renda, A. Cipollina, G. Micale, M. Ciofalo, Investigation of heat transfer in spacer-filled channels by experiments and direct numerical simulations, *Int. J. Heat Mass Transfer*, 93 (2016) 1190-1205.

[12] A. Mahdavifar, A. Pollard, J.G. Pharoah, S.B. Beale, Wall proximity effects on flow over a simple membrane spacer, *Computers & Fluids*, 88 (2013) 180–188.

[13] S. M. Mojab, A. Pollard, J.G. Pharoah, S.B. Beale, E.S. Hanff, Unsteady Laminar to Turbulent Flow in a Spacer-Filled Channel, *Flow Turbulence Combust.*, 92 (2014) 563–577.

[14] M. Shakaib, S.M.F. Hasani, I. Ahmed, R.M. Yunus, A CFD study on the effect of spacer orientation on temperature polarization in Membrane Distillation modules, *Desalination*, 284 (2012) 332–340.

[15] M. Gimmelshtein, R., Semiat, Investigation of flow next to membrane walls, *J. Memb. Sci.*, 264 (2005) 137-150.

[16] A. R. Da Costa, A. G. Fane, D. E. Wiley, Spacer characterization and pressure drop modelling in spacer filled channel for ultrafiltration, *J. Membr. Sci.*, 87 (1994) 79-98.

[17] J. Liu, A. Iranshahi, Y. Lou, G. Lipscomb, Static mixing spacers for spiral wound modules, *J. Membr. Sci.*, 442 (2013) 140–148.

[18] T. Melin, New ED - Advanced Bipolar Membrane Processes for Remediation of Highly Saline Waste-water Streams, *Proc. Nano4water Workshop*, 26 October 2010.

[19] F. Ponzio, A. Tamburini, A. Cipollina, G. Micale, M. Ciofalo, Experimental and computational investigation of heat transfer in channels filled by woven spacers, Submitted to *Int. J. Heat Mass Transfer*, 2016.

[20] A. Tamburini, A. Parlapiano, A. Cipollina, M. Ciofalo, G. Micale, Temperature distribution analysis in spacer filled channels for Membrane Distillation, Procs. 7th Int. Symp. *Turbulence, Heat and Mass Transfer*, Palermo, Italy, 24-27 September 2012, pp. 299-302, K. Hanjalic, Y. Nagano, D. Borello and D. Jakirlic, eds, Begell House Inc., New York, 2012.

[21] S. Al-Sharif, M. Albeirutty, A. Cipollina, G. Micale, Modelling flow and heat transfer in spacer-filled Membrane Distillation channels using open source CFD code, *Desalination*, 311 (2013) 103-112.

[22] A. Tamburini, G. Micale, M. Ciofalo, A. Cipollina, Experimental analysis via Thermochromic Liquid Crystals of the temperature local distribution in Membrane Distillation modules, *Chem. Eng. Trans.* 32 (2013) 2041-2046.

[23] A. Tamburini, P. Pitò, A. Cipollina, G. Micale, M. Ciofalo, A Thermochromic Liquid Crystals image analysis technique to investigate temperature polarization in spacer-filled channels for membrane distillation, *J. Membr. Sci.*, 447 (2013) 260-273.

[24] M. Ciofalo, I. Di Piazza, J. A. Stasiek, Investigation of flow and heat transfer in corrugated-undulated plate heat exchangers, *Heat and Mass Transfer*, 36 (2000) 449-462.

[25] M. Ciofalo, M. Signorino, M. Simiano, Tomographic Particle Image Velocimetry and Thermography in Rayleigh-Bènard convection using suspended Thermochromic Liquid Crystals and Digital Image Processing, *Experiments in Fluids*, 34 (2003) 156-172.

[26] A. Tamburini, G. La Barbera, A. Cipollina, M. Ciofalo, G. Micale, CFD simulation of channels for direct and reverse Electro Dialysis, *Desalination and Water Treatment*., 48 (2012) 370-389.

[27] Ansys Inc., *Ansys-CFX Reference Guide, Release 14.5* (2012).

[28] F. R. Menter, Two-equation eddy-viscosity turbulence models for engineering applications, *AIAA Journal*, 32 (1994) 269–289.

[29] I. Di Piazza, M. Ciofalo, Numerical prediction of turbulent flow and heat transfer in helically coiled pipes, *Int. J. Thermal Sci.*, 49 (2010) 653-663.